Journal of Colloid and Interface Science 532 (2018) 375–386

Contents lists available at ScienceDirect

Journal of Colloid and Interface Science

journal homepage: www.elsevier.com/locate/jcis

Regular Article

Bismuth oxyfluoride/bismuth oxyiodide nanocomposites enhance visible-light-driven photocatalytic activity

Chiing-Chang Chen *, Jing-Ya Fu, Jia-Lin Chang, Shiuh-Tsuen Huang, Tsung-Wen Yeh, Jiun-Ting Hung, Peng-Hao Huang, Fu-Yu Liu, Li-Wen Chen *

Department of Science Education and Application, National Taichung University of Education, Taichung 403, Taiwan

GRAPHICAL ABSTRACT

Schematic of the band-gap structures of BiOF/BiOI and the possible charge separation processes.

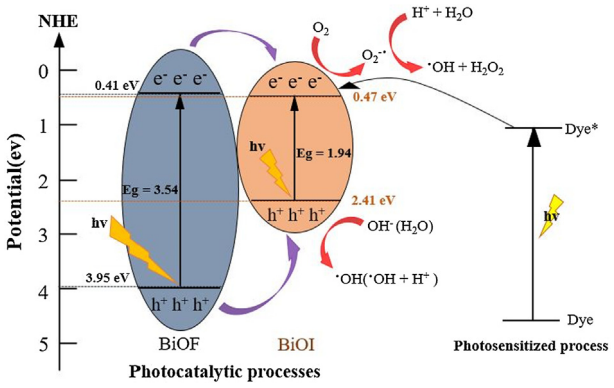

ARTICLE INFO

Article history:
Received 10 June 2018
Revised 26 July 2018
Accepted 29 July 2018
Available online 3 August 2018

Keywords:
BiOF
BiOI
Nanocomposites
Photocatalytic
Crystal violet
2-Hydroxybenzoic acid

ABSTRACT

This is the first paper to report a series of bismuth oxyfluoride/bismuth oxyiodide (BiO_pF_q/BiO_xI_y) nanocomposites with different F/I molar ratios, pH values, and reaction temperatures that were synthesized through a template-free and controlled hydrothermal method. These nanocomposites were characterized through scanning electron microscope energy dispersive microscopy (SEM-EDS), transmission electron microscopy (TEM), X-ray diffraction (XRD), Fourier-transform infrared (FT-IR), X-ray photoelectron spectroscopy (XPS), Brunauer–Emmett–Teller (BET), and diffuse reflectance spectroscopy (DRS). Under visible-light irradiation, the BiO_pF_q/BiO_xI_y composites exhibited excellent photocatalytic activities in the degradation of crystal violet (CV) and 2-hydroxybenzoic acid (HBA). The order of rate constants was BiOF/BiOI > BiOI ≫ BiOF. The photocatalytic activity of BiOF/BiOI composites reached a maximum rate constant of 0.2305 h^{-1}, 1.2 times higher than that of BiOI and 100 times higher than that of BiOF. Thus, the derived BiOF/BiOI is crucial for photocatalytic activity enhancement. After the removal of CV in the third cycle, no apparent deficits in photocatalytic activity were observed, and the observed deficit was 8.2% during the fifth run. Overall, the catalytic activity and stability observed for the proposed composites were determined to be adequate under visible-light irradiation. For various scavengers, the noted quenching effects demonstrated that reactive O_2^- has a notable role in the degradation of the applied CV.

* Corresponding authors.
E-mail addresses: ccchen@mail.ntcu.edu.tw (C.-C. Chen), liwenchen@mail.ntcu.edu.tw (L.-W. Chen).

https://doi.org/10.1016/j.jcis.2018.07.130
0021-9797/

1. Introduction

Scholars have devoted considerable attention to semiconductor photocatalysis energized by visible light, because this is an effective approach to overcome problems linked to environmental pollution and energy production. A photocatalyst that is effective, low-cost, and environmentally friendly is paramount for practical photocatalysis applications [1]. Relevant research has focused primarily on the elimination of toxic constituents from wastewater. Scholars have used various systems to photodegrade crystal violet (CV) dyes and thus to produce active species such as BiO_xCl_y/BiO_mI_n [2], BiOBr/BiOI [3], $BaTiO_3$ [4], BiOI [5], Bi_2WO_6 [6], $PbBiO_2Br/BiOBr$ [7], BiOI/GO [8], $Bi_2SiO_5/g\text{-}C_3N_4$ [9], and $SrFeO_{3-x}/g\text{-}C_3N_4$ [10]. The incorporation of heterostructures can effectively improve a photocatalyst's photocatalytic activity in a facile manner; this strategy may enable tuning photocatalyst electronic properties to particular desired levels and efficient photoinduced electron–hole pair separation.

Bismuth oxyhalide compounds (BiOX, X = F, Cl, Br, and I) offer remarkable chemical stability, uniquely layered structures, and highly favorable photocatalytic performance under UV–Vis illumination. Scholars have increasingly published studies of some noteworthy characteristics of BiOX, namely favorable energy gaps, high stability, and photocatalytic activity levels superior to those of other compounds [11,12]. The bandgaps of BiOF [13], $Bi_xO_yF_z$ [14], BiOCl/BiOF [15], and BiOBr/BiOF [16] have been reported to be 3.64, 3.35–3.44, 3.56 eV, and 3.85 eV, respectively. Among these compounds, BiOF has a direct bandgap of nearly 3.5 eV; therefore BiOF is a photocatalyst that is sensitive to UV radiation. The atomic structure of BiOF has layers of $[Bi_2O_2F_2]$ because $[Bi_2O_2]^{2+}$ slabs are positioned between pairs of fluorine atoms $[F_2]^{2-}$ [13,14]. The valence band of bismuth oxyiodides is mostly composed of I_{5p} and O_{2p} orbitals, whereas the Bi_{6p} orbital comprises the conduction band [17]; thus, the bandgap energy of iodine-poor BiO_mI_n is lower compared with Bi_2O_3 but higher compared with BiOI [18]. Therefore, these materials may be effective as visible-light photocatalysts. Specifically, the structure and composition of BiO_mI_n strongly affect its physicochemical characteristics such as oxidizing abilities, optical characteristics, and electronic characteristics; thus, novel photocatalysts may be developed for the effective degradation of environmental and toxic pollutants. Keller and Kramer reported on BiOX/BiOY systems (X, Y = Cl, Br, and I) that demonstrated nearly unlimited solubility [19]; since that report, scholars have published papers regarding syntheses of similar oxyhalide materials with special photocatalytic activities. Recently, the literature has grown with numerous reports of BiOX/BiOY synthesis approaches, characterizations, and assessed features.

Per the authors' review of relevant literature, no study has examined the use of visible-light irradiation for photocatalytic degradation of CV dyes with the aid of BiO_pF_q/BiO_xI_y. This study employed a template-free and controlled hydrothermal method to synthesize a series of BiO_pF_q/BiO_xI_y nanocomposites with different F/I molar ratios, pH values, and reaction temperatures; moreover, this study compared the photocatalytic activities of these compounds in terms of CV degradation in aqueous media under visible-light irradiation. This paper puts forth and explains some mechanisms that may trigger photodegradation. The present study contributes methods for synthesizing BiO_pF_q/BiO_xI_y and degrading organic compounds; in the future, these methods may be applied for the mitigation of environmental pollution.

2. Experiment

2.1. Materials

All chemicals utilized in this study were of analytic grade, with no additional purification. The following additional materials were purchased: HBA (2-hydroxybenzoic acid or salicylic acid), $Bi(NO_3)_3{\cdot}5H_2O$, KI, KF (Katayama), KCl (Shimakyu), CV dye (TCI), sodium azide (Sigma), *p*-benzoquinone (Alfa Aesar), isopropanol (Merck), and ammonium oxalate (Osaka). Reagent-grade ammonium acetate, sodium hydroxide, nitric acid, and HPLC-grade methanol were obtained from Merck.

2.2. Instruments and analytical methods

A diffractometer system (MAC Science MXP18) applying Cu–Kα radiation (40 kV and 80 mA) recorded XRD patterns. XPS was recorded with an ULVAC-PHI spectrometer. Al–Kα radiation was realized at 15 kV; a Scinco SA-13.1 spectrophotometer recorded UV–Vis-DRS data within the 300–800 nm wavelength range at room temperature. SEM-EDS was performed using a JEOL JSM-7401F microscope, with the acceleration voltage set to 15 kV. Moreover, a JEOL-2010 microscope was utilized to obtain TEM images, EDS spectra, high-resolution TEM images, and selected-area electron diffraction patterns, with the acceleration voltage being set at 200 kV. An automated system (Micromeritics Gemini) recorded the samples' BET specific surface areas (S_{BET}) at 237 °C; in this process, nitrogen gas was utilized as the adsorbate at liquid-nitrogen temperature. UV photoelectron spectroscopy data were collected with an ULVAC-PHI XPS PHI Quantera SXM, and PL data were obtained with a Hitachi F-7000. Finally, a Brüker ER200D spectrometer, with an Agilent 5310A frequency counter operating in the X band, recorded EPR spectra at 77 K.

2.3. Synthesis of BiO_pF_q/BiO_xI_y

A 50-mL flask was filled with 5 mmol $Bi(NO_3)_3{\cdot}5H_2O$, after which 5 mL 4 M HNO_3 was added. The contents of the flask were continuously stirred, with the addition of 2 M NaOH dropwise for realizing pH value adjustment. After the observation of precipitate formation, 3 M portions of KF and KI (with various KF:KI molar ratios) were added dropwise. The solution underwent 30 min of vigorous stirring, followed by transferring it to a 30 mL Teflon-lined stainless-steel autoclave; next, the autoclave was exposed to heating temperatures ranging from 100 to 250 °C for 12 h, and it was subsequently allowed to cool to room temperature. After these processes, the solid obtained was collected to filtration, washing performed using deionized water and ethanol for ionic species removal, and then overnight dried at 80 °C. A selection of BiO_pF_q/BiO_xI_y composites were prepared with controlled values of KF:KI molar ratio (1:2 or 2:1), temperature (100–250 °C), pH (1–14), and reaction times (12 h), as indicated in Table 1. The as-prepared samples were named with identifiers sequentially from BF1I2-1-100 to BF2I1-14-250.

2.4. Photocatalytic and active species experiments

In the trials of this study, we chose either CV (or HBA) as our target pollutant to evaluate photocatalytic activity. CV (or HBA) irradiation products were immersed in stirred aqueous solutions housed in flasks (100 mL); both an aqueous dispersion of 10 ppm 100 mL CV (or HBA) and 10 mg of the photocatalyst were then placed in a Pyrex flask. The suspension's pH was adjusted through the addition of sodium hydroxide or nitric acid solution addition. Following batch sorption experiments, the mixture was subjected to a centrifugation procedure conducted at 3000 rpm to determine the absorbance of CV (or HBA) at 585 (or 300) nm through HPLC-PDA. The optical system for the catalytic reaction under visible-light includes a 10 W Xe arc lamp, a reaction container and a cut-off filter ($\lambda > 420$ nm), with the light intensity fixed at 3.2 W/m^2 for irradiating the reaction vessel 30 cm away from the light source. At specified irradiation time intermissions, 5-mL aliquots were

Table 1
Codes of as-prepared samples under different hydrothermal conditions. (Hydrothermal conditions: molar ratio KF/KI = 1/2–2/1, temp = 100–250 °C, pH = 1–14, time = 12 h).

Molar ratio (F:I = 1:2) pH value	Temperature (°C) 100	150	200	250
1	BF1I2-1-100	BF1I2-1-150	BF1I2-1-200	BF1I2-1-250
4	BF1I2-4-100	BF1I2-4-150	BF1I2-4-200	BF1I2-4-250
7	BF1I2-7-100	BF1I2-7-150	BF1I2-7-200	BF1I2-7-250
10	BF1I2-10-100	BF1I2-10-150	BF1I2-10-200	BF1I2-10-250
13	BF1I2-13-100	BF1I2-13-150	BF1I2-13-200	BF1I2-13-250
14	BF1I2-14-100	BF1I2-14-150	BF1I2-14-200	BF1I2-14-250
Molar ratio (F:I = 2:1) pH value	Temperature (°C) 100	150	200	250
1	BF2I1-1-100	BF2I1-1-150	BF2I1-1-200	BF2I1-1-250
4	BF2I1-4-100	BF2I1-4-150	BF2I1-4-200	BF2I1-4-250
7	BF2I1-7-100	BF2I1-7-150	BF2I1-7-200	BF2I1-7-250
10	BF2I1-10-100	BF2I1-10-150	BF2I1-10-200	BF2I1-10-250
13	BF2I1-13-100	BF2I1-13-150	BF2I1-13-200	BF2I1-13-250
14	BF2I1-14-100	BF2I1-14-150	BF2I1-14-200	BF2I1-14-250

collected and subjected to centrifugation for photocatalyst removal, and each supernatant sample was subsequently analyzed through HPLC-PDA.

A series of quenchers were introduced to scavenge the relevant active species to evaluate the effect of the active species during the photocatalytic reaction. Superoxide radicals ($O_2^{\cdot-}$), hydroxyl radicals ($^{\cdot}OH$), holes (h^+), and singlet oxygen ($^1O_2$) were studied by adding 1.0 mM benzoquinone (BQ; a quencher of $O_2^{\cdot-}$), 1.0 mM isopropanol (IPA; a quencher of $^{\cdot}OH$), 1.0 mM ammonium oxalate (AO; a quencher of h^+), and 1.0 mM sodium azide (SA, a quencher of $^1O_2$). The method was similar to that of a previously reported photocatalytic activity test [2,3].

3. Results and discussion

3.1. Characterization of BiO_pF_q/BiO_xI_y composites

3.1.1. Xrd

Fig. 1 and Fig. S1 of the supplementary data depict the as-prepared samples' XRD patterns, evidencing different BiO_pF_q/BiO_xI_y phase composites. These results indicated the BiOF phase in all as-prepared samples (JCPDS 73-1595), $Bi_{50}O_{59}F_{32}$ phase (JCPDS 24-0145), $Bi_{26}O_{38}F_2$ phase (JCPDS 41-0617), BiOI phase (JCPDS 10-0445), $Bi_7O_9I_3$ phase [20], and Bi_5O_7I phase (JCPDS 40-0548) [21]. The XRD patterns were the same as those obtained for BiOF/BiOI, $Bi_{50}O_{59}F_{32}$/BiOI, $Bi_{26}O_{38}F_2/Bi_5O_7I$, binary phases and $Bi_{26}O_{38}F_2$/BiOI/Bi_5O_7I, BiOF/BiOI/Bi_2O_3, as well as $Bi_{26}O_{38}F_2/Bi_5O_7I$/β-$Bi_2O_3$ ternary phases. The XRD data derived at various F/I molar ratios, pH values and reactions are listed in Table 2. The results proved that a series of changes occurred in the products at specific pH values. The changes, expressed as BiOF → $Bi_{50}O_{59}F_{32}$ → $Bi_{26}O_{38}F_2$ → Bi_2O_3 and as BiOI → $Bi_4O_5I_2$ → $Bi_7O_9I_3$ → Bi_3O_4I → Bi_5O_7I → Bi_2O_3, occurred under various hydrothermal conditions. By changing the pH of the hydrothermal reaction, various bismuth oxyhalide compositions were synthesized. In these experiments, pH played a key role, whereas molar ratio and temperature played a minor role in controlling the composition and anisotropic growth of crystals. Overall, the controllable morphologies and crystal phases of bismuth oxyhalide could be completed by simply changing some growth parameters, for example, pH and molar ratio. Chen et al. also demonstrated that the synthesis of a series bismuth oxyhalides structures by using a hydrothermal autoclave at different X/Y (X, Y = Cl, Br, I) molar ratio, pH values and reaction resulted in higher photocatalytic efficiency toward CV, phenol, and HBA

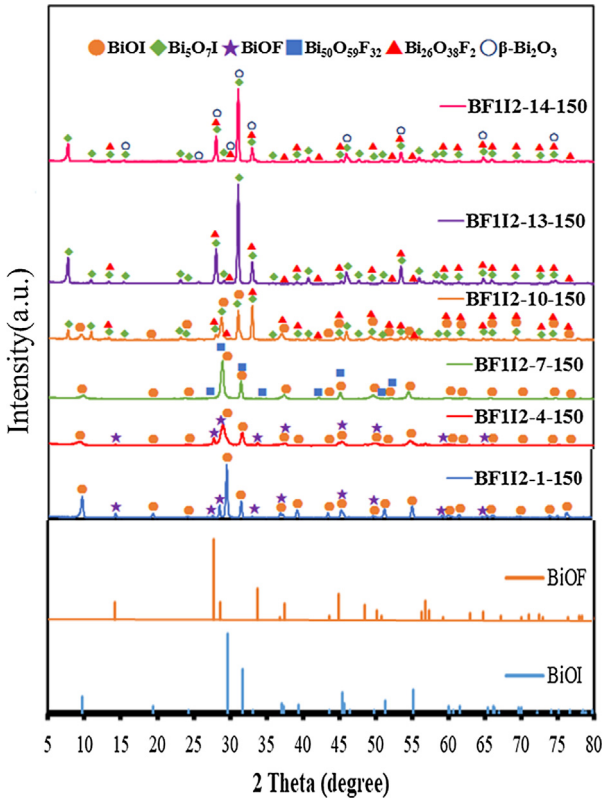

Fig. 1. XRD patterns of as-prepared BiO_pF_q/BiO_xI_y samples at different pH values (hydrothermal conditions: molar ratio KF/KI = 1/2; Temp = 150 °C; Time = 12 h).

under visible-light irradiation [2,3,5,22–24]. Some reactions that may have caused the formation of the BiO_pF_q/BiO_xI_y as-samples are formalized as Eqs. (1)–(14):

Supplementary data associated with this article can be found, in the online version, at https://doi.org/10.1016/j.jcis.2018.07.130.

$$Bi^{3+} + 3\ OH^- \rightarrow Bi(OH)_3\ (s) \quad (1)$$

$$Bi(OH)_3\ (s) + 3F^- \rightarrow BiF_3\ (s) + 3\ OH^- \quad (2)$$

$$BiF_3\ (s) + 2\ OH^- \rightarrow BiOF\ (s) + 2F^- + H_2O \quad (3)$$

Table 2
Crystalline phase changes of as-prepared samples under different hydrothermal conditions. (Hydrothermal conditions: molar ratio KF/KI = 1/2–2/1, temp = 100–250 °C, pH = 1–14, time = 12 h). ●BiOI ◆Bi_5O_7I ★BiOF ■$Bi_{50}O_{59}F_{32}$ ▲$Bi_{26}O_{38}F_2$ ▼Bi_2O_3 ○β-Bi_2O_3.

Molar ratio (F : I = 1 : 2)	Temperature (°C)			
pH value	100	150	200	250
1	●★	●★	●★	●★
4	●■	●★	●★	●★
7	●■	●■	●■	●★
10	●◆▲	●◆▲	●◆▲	●◆▲
13	◆▲	◆▲	◆▲	◆▲
14	●★▼	◆▲○	◆▲○	◆▲○
Molar ratio (F : I = 2 : 1)	**Temperature (°C)**			
pH value	100	150	200	250
1	●★	●★	●★	●★
4	●★	●★	●★	●★
7	●■	●■	●■	◆★
10	◆▲	◆▲	◆▲	◆▲
13	◆▲	◆▲	◆▲	◆▲
14	◆▲○	◆▲○	◆▲○	◆▲○

$$50BiOF\ (s) + 18\ OH^- \rightarrow Bi_{50}O_{59}F_{32}\ (s) + 18F^- + 9H_2O \quad (4)$$

$$13Bi_{50}O_{59}F_{32}\ (s) + 366\ OH^- \rightarrow 25Bi_{26}O_{38}F_2\ (s) + 366F^- + 183H_2O \quad (5)$$

$$Bi_{26}O_{38}F_2\ (s) + 2\ OH^- \rightarrow 13\ Bi_2O_3\ (s) + 2F^- + H_2O \quad (6)$$

$$2Bi(OH)_3\ (s) + I^- \rightarrow BiOI\ (s) + H_2O + OH^- \quad (7)$$

$$Bi^{3+} + 3\ I^- \rightarrow BiI_3\ (s) \quad (8)$$

$$BiI_3\ (s) + 2\ OH^- \rightarrow BiOI\ (s) + 2\ I^- + H_2O \quad (9)$$

$$4\ BiOI\ (s) + 2\ OH^- \rightarrow Bi_4O_5I_2\ (s) + 2\ I^- + H_2O \quad (10)$$

$$7\ Bi_4O_5I_2\ (s) + 2\ OH^- \rightarrow 4\ Bi_7O_9I_3\ (s) + 2\ I^- + H_2O \quad (11)$$

$$3\ Bi_7O_9I_3\ (s) + 2\ OH^- \rightarrow 7\ Bi_3O_4I\ (s) + 2\ I^- + H_2O \quad (12)$$

$$5\ Bi_3O_4I\ (s) + 2\ OH^- \rightarrow 3\ Bi_5O_7I\ (s) + 2\ I^- + H_2O \quad (13)$$

$$2\ Bi_5O_7I\ (s) + 2\ OH^- \rightarrow 5\ Bi_2O_3\ (s) + 2\ I^- + H_2O \quad (14)$$

These equations indicate that at or near the beginning of the reaction, BiOF (or BiOI) manifested, and that OH^- ions gradually were substituted for F^- (or I^-) ions under the fundamental conditions; thus, the products contained reduced amounts of F^- (or I^-) ions. The progress of the BiO_pF_q/BiO_xI_y hydrothermal synthesis can be tracked by monitoring the F^- and I^- ions formed in the solution by using a bi-halo-semiconductor. These results suggested that OH^- ions displaced F^- and I^- ions slowly with increase in the applied pH value, due to which the system produced BiOF, $Bi_{50}O_{59}F_{32}$, $Bi_{26}O_{38}F_2$ (or BiOI, $Bi_4O_5I_2$, $Bi_7O_9I_3$, Bi_3O_4I, Bi_5O_7I), and Bi_2O_3; that is, high pH values were correlated with products that had low F^- (or I^-) concentrations. In the final products, OH^- ions completely replaced the F^- (or I^-) ions, and thus Bi_2O_3 formed under strong basic conditions. The relationships between OH^-, F^-, and I^- existing in aqueous solutions are typically competitive. In this study, a hydrothermal method was applied for the selective preparation of BiO_pF_q/BiO_xI_y through control of the pH value, the molar ratio, and the reaction temperature.

3.1.2. SEM and TEM

In this study, the hydrothermal method was applied at various pH values to yield a series of BiO_pF_q/BiO_xI_y composites, whose surface morphologies were examined through the use of FE-SEM-EDS. Fig. 2(a) and Fig. S2 present the derived TEM and FE-SEM images for these samples, revealing small-thin nanosheet, nanosheet, square-plate, flower-like, irregular small-thin nanosheet, and rods morphologies. The derived samples primarily comprised bismuth, oxygen, fluorine, and iodine, as demonstrated by SEM-EDS (Tables S1 and S2). Thus, the controlled hydrothermal method could be applied for synthesizing, through a selective process, a series of BiO_pF_q/BiO_xI_y composites. As evidenced by high-resolution transmission electron microscopy (Fig. 2(c) and (d)), two lattice image sets were found, wherein the associated d-spacing was 0.2649 and 0.3011 nm, which corresponded to the (1 1 2) plane of BiOF and the (1 1 0) plane of BiOI, an adequately concordant outcome with the XRD results (Fig. 1). Our group [2,3,5] revealed that the controllable morphologies and crystal phases of bismuth oxyhalides could be completed by simply changing some growth parameters, including pH values, molar ratio, and hydrothermal temperature. BiOF and BiOI were obtained at low pH values; $Bi_{50}O_{59}F_{32}$ and $Bi_7O_9I_3$ were obtained at mid-level pH values; $Bi_{26}O_{38}F_2$ and Bi_5O_7I were obtained at high pH values. This reference demonstrated that BiOF and BiOI were formed at the beginning of the hydrothermal reaction, and then OH^- gradually substituted F^- and I^- in the basic conditions; this initially resulted in the reduced content of F^- and I^- in the samples and eventually resulted in the formation of Bi_2O_3 under strong basic conditions. The detailed statements about the effect of reaction temperature and molar

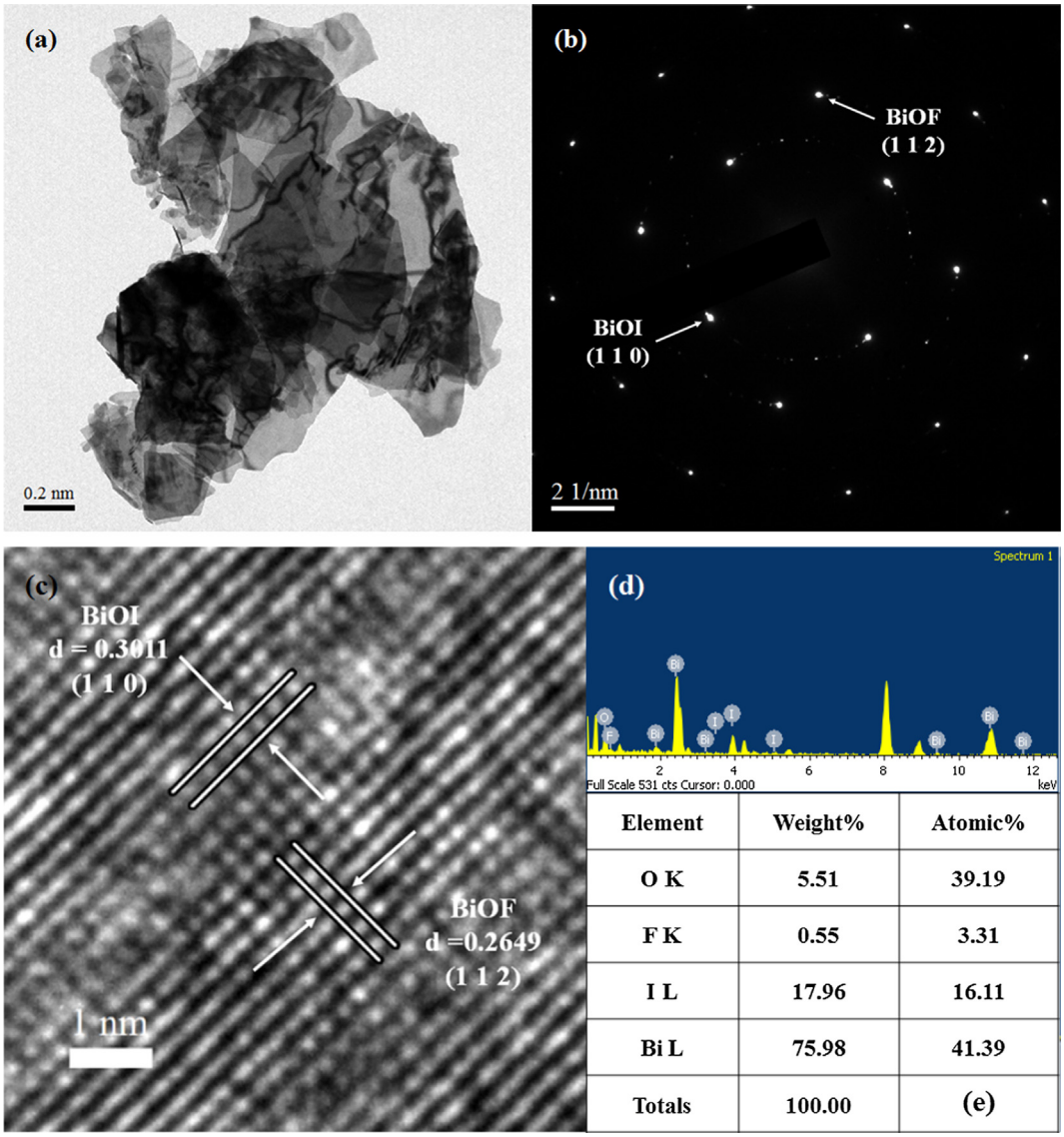

Element	Weight%	Atomic%
O K	5.51	39.19
F K	0.55	3.31
I L	17.96	16.11
Bi L	75.98	41.39
Totals	100.00	(e)

Fig. 2. (a) TEM image, (b) SAD, (c) HR-TEM image, (d) EDS, and (e) atomic ratio of BiOF/BiOI (BF1I2-4-150) sample prepared using the hydrothermal autoclave method.

ratio are described in the Refs. [2,3,5]. A series of bismuth oxyfluoride/bismuth oxyiodide phases were synthesized in the composites, as suggested by the results, and the synthesized phases facilitated separating the corresponding photoinduced carriers, thereby engendering high photocatalytic activity levels.

3.1.3. Xps

The purity levels of the synthesized samples were characterized through XPS. Fig. 3 depicts Bi 4f, O 1s, F 1s, and I 3d spectra from the BiOF/BiOI sample. The transition peaks involved in the orbitals of these spectra indicate that Bi, O, F, and I were catalysts. The distinctive binding energy values derived for Bi $4f_{7/2}$ were 155.6 and 158.0 eV for BiOI and BiOF (Fig. 3(a)), indicating a trivalent oxidation state for bismuth. Liao et al. [2,5] have published a similar binding energy for Bi $4f_{7/2}$. Fig. 3(b) depicts high-resolution XPS spectra that were recorded for the BiOF/BiOI composites' O 1s region; this spectra were resolved into a main peak and a secondary peak. The main peak (528.8 eV) can be attributed to the Bi–O bonds in the $(Bi_2O_2)^{2+}$ slabs. The secondary peak (530.5 eV) can be assigned to the hydroxyl groups on the surface [25]. The binding energy for F 1s was 679.2 eV, as presented in Fig. 3(c); this can be ascribed to F existing in a monovalent oxidation state. Binding energies of 618.0 and 629.7 eV were derived for I $3d_{5/2}$ and $3d_{3/2}$, respectively, as depicted in Fig. 3(d) and can be ascribed to I existing in a monovalent oxidation state.

3.1.4. Drs

Fig. 4 and Fig. S3 illustrate UV–Vis absorption spectra from various BiO_pF_q/BiO_xI_y composites. E_g of BiO_pF_q/BiO_xI_y was calculated to be in the range of 1.78–2.99 eV with a plot of $(\alpha h\nu)^{1/2}$ against energy ($h\nu$). Similar plots of $(\alpha h\nu)^{1/2}$ against energy ($h\nu$) revealed the E_g values of BiOF, BiOI, and BiOF/BiOI to be 3.47, 1.91, and 2.05 eV, respectively. The evidence indicates that the fabricated BiO_pF_q/BiO_xI_y composites had considerably enhanced optical absorption characteristics and solar light efficiency; therefore these composites would be excellent photocatalysts.

3.1.5. Bet

Fig. 5 presents isotherm curves derived by plotting nitrogen adsorption against nitrogen desorption for BiOF/BiOI. In the relatively high pressure range of 0.8–1.0, a hysteresis loop similar to H3 was evident, and BiOF/BiOI isotherms were found to approximate Type IV isotherms [2]. The fact that the hysteresis loop's shape resembled that of H3 suggests the presence of pores. These

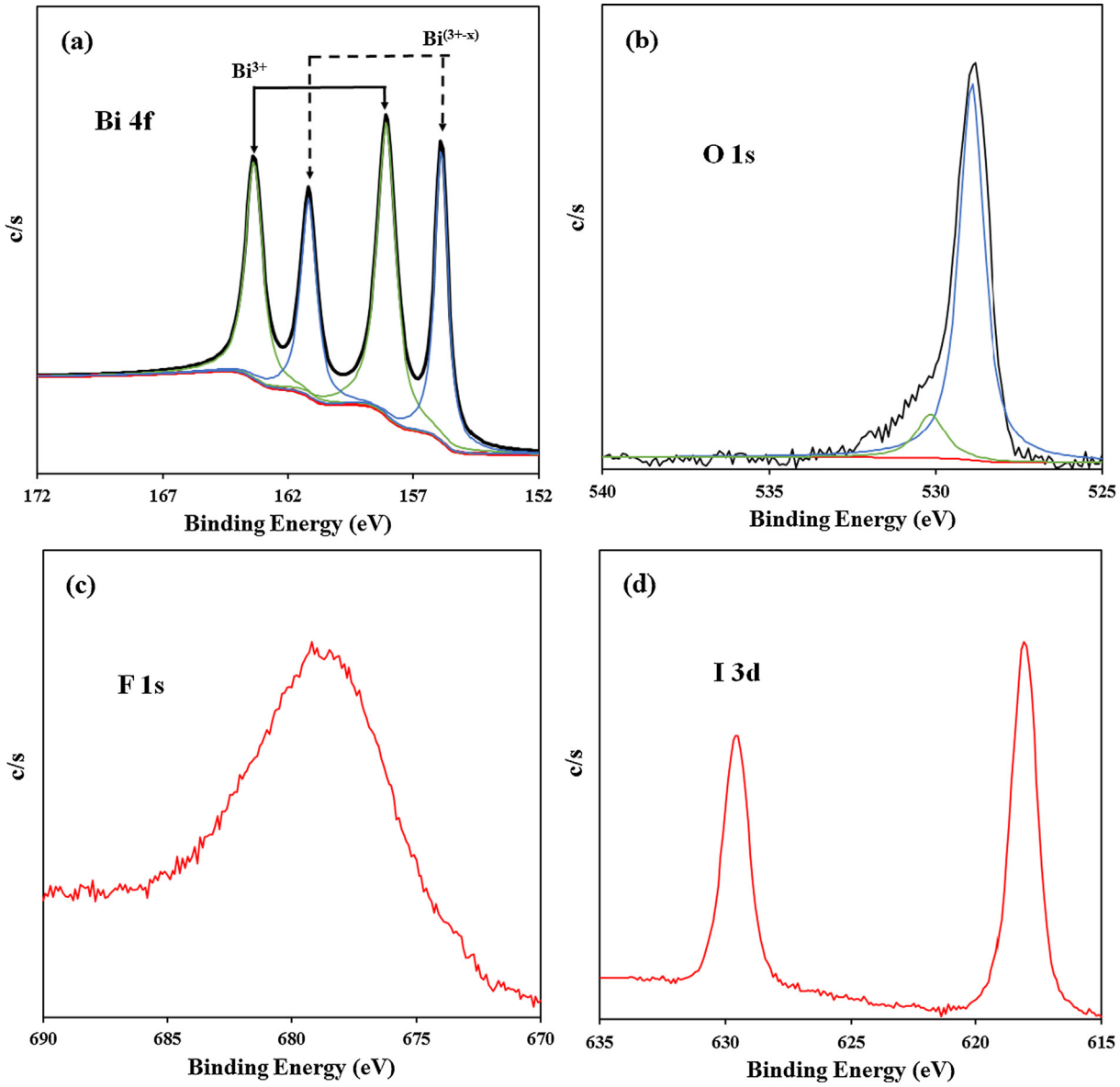

Fig. 3. High-resolution XPS spectra of as-prepared BiOF/BiOI (BF1I2-4-150) sample. (a) Bi 4f; (b) O 1s; (c) F 1s; (d) I 3d.

pores resembled slits; such slits are typically formed by aggregating sheets or plates. This finding is consistent with the FE-SEM data as well as the nanosheet and nanoplate morphologies of the self-assembled samples. Thus, these self-assembled nanosheets formed hierarchical architectures. From Table 3, the BET surface area of the sample was 11.33 $m^2 g^{-1}$. Pore volume and diameter values of 0.066 cm^3/g and 3157 nm, respectively, were calculated for BiOF/BiOI. Besides, the BET surface area of BiOF and BiOI were 6.4 and 2.1 $m^2 g^{-1}$. Pore volume and diameter values of 0.071 and 0.019 cm^3/g and 5771 and 4237 nm, respectively.

Fig. 5 (inset) shows the corresponding pore-size dis-tribution (PSD) of BiOF/BiOI. The PSD curves are di-modal for the samples, indicating medium mesopores (10–30 nm) and large macropores (100–2000 nm). Because the nanosheets do not contain pores (Fig. 2(a) and Fig. S2 of supplementary data), the medium mesopores may reflect porosity within nanosheets. The large macrop-ores may attribute to the pores formed between stacked nanosheets, while the large macropores may be ascribed to the pores formed between nanosheets. Such self-organized porous architectures may be extremely useful in photocatalysis because they provide efficient transport pathways for reactant and product molecules.

3.2. Photocatalytic activity

3.2.1. UV–Vis spectra

Fig. 6 illustrates the changes of the UV–Vis spectra during CV and HBA visible-light photodegradation in aqueous BiOF/BiOI dispersions. Fig. 6(a) presents that approximately 99% of the CV degraded after 24 h of visible-light irradiation. The characteristic CV dye absorption band is graphed at around 588.9 nm. When the dye was irradiated with visible light, the band rapidly decreased and small hypsochromic shifts (543.1 nm) were observed; no additional absorption band was observed; no band was observed in the UV range ($\lambda > 200$ nm); therefore, the visible-light irradiation of CV formed a sequence of *N*-demethylated intermediates. The entirety of the CV dye's conjugated chromophore structure might have undergone cleavage. When the sample was irradiated with additional visible light, the absorption band at 543.1 nm was diminished; however, no additional shift in

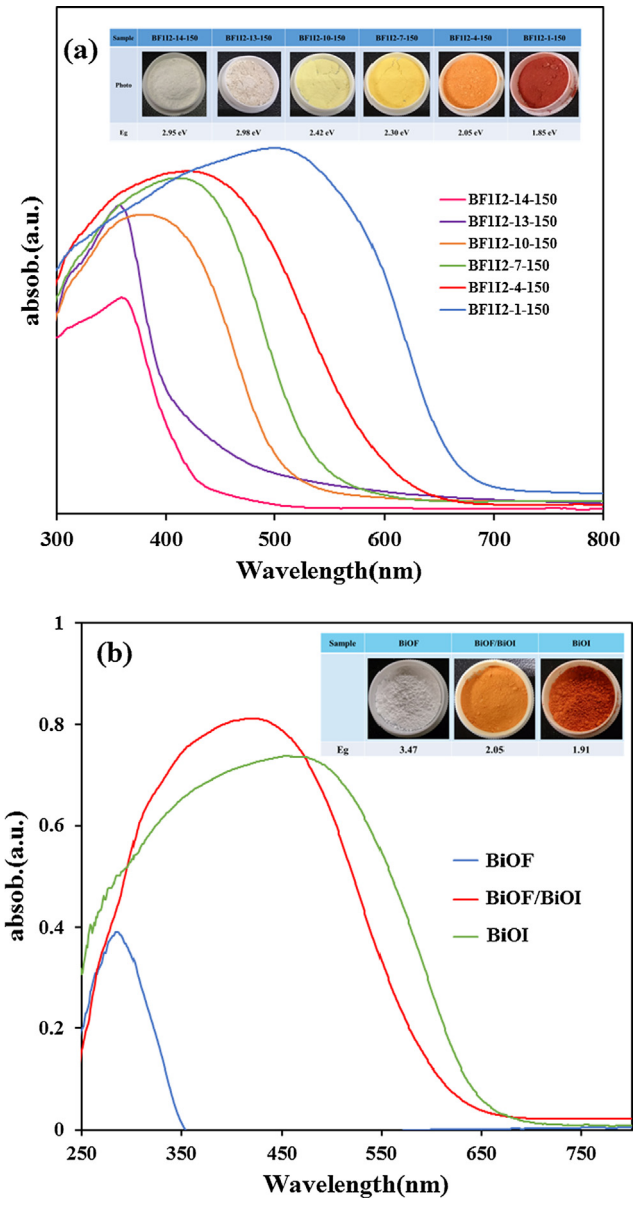

Fig. 4. UV–vis absorption spectra of the (a) as-prepared photocatalysts under different pH values (Molar ratio KF/KI = 1/2; Temp = 150 °C; Time = 12 h), and (b) BiOF, BiOF/BiOI, and BiOI.

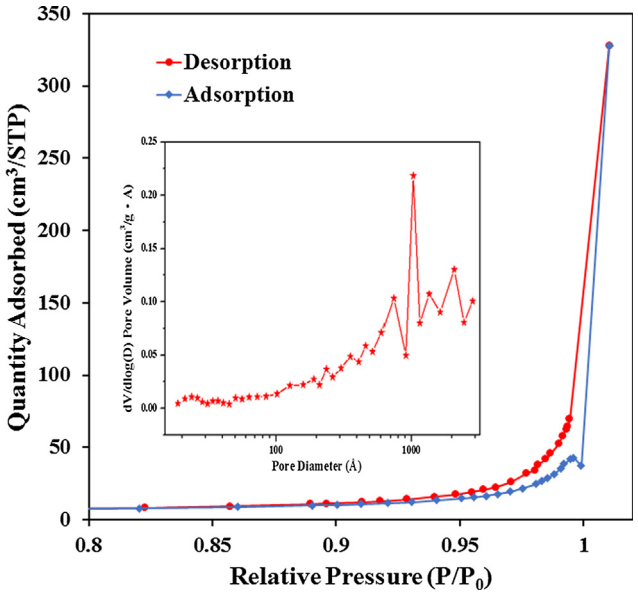

Fig. 5. N_2 adsorption–desorption isotherm distribution curves and (inset) the pore distribution curves for BiOF/BiOI (hydrothermal conditions: molar ratio KF/KI = 1/2; temp = 150 °C; time = 12 h).

Table 3
Physical and chemical properties of as-prepared samples at different conditions (Hydrothermal conditions: molar ratio KF/KI = 1/2, temp = 150 °C, pH = 1–14, time = 12 h).

Sample	BET surface area (m^2/g)	Pore diameter (nm)	Pore volume (cm^3/g)
BF1I2-1-150	0.4277	4623.50	0.306176
BF1I2-4-150	11.3252	3157.18	0.066026
BF1I2-7-150	3.3168	4657.88	0.034334
BF1I2-10-150	2.7179	4536.63	0.157513
BF1I2-13-150	1.3955	5705.56	0.009095
BF1I2-14-150	0.6667	5681.25	0.004460

wavelength was observed; therefore, this absorption band (i.e., 543.1 nm) can be considered the band of the whole *N*-demethylated product of the CV dye [2,6]. After 144 h of irradiation, the BiOF/BiOI composites demonstrated superior photocatalytic performance, with the removal efficiency observed for HBA reaching 85% (Fig. 6(b)). These values notably exceeded those of other composites synthesized in this study, indicating that the BiOF/BiOI for CV and HBA degradation were much more effective photocatalysts. It should be noticed that the degradation of CV only takes about only 1/10 of the reaction time for the degradation of HBA. The possible reason is the photosensitization degradation of CV dye [16]. Jiang et al. [16] have published a similar result.

3.2.2. Degradation efficiency

Degradation efficiency is graphed against reaction time in Fig. 6 (c), (d) and Fig. S4; using 0.05 g of BiO_pF_q/BiO_xI_y enhanced removal efficiency substantially. To elucidate the reaction kinetics controlling CV degradation, an apparent pseudo–first-order model [26], namely $\ln(C_o/C) = kt$, was employed in the experiments. The data in Table 4 were fit to a first-order linear fit; consequently, the k value of the BiOF/BiOI composite, BiOF, and BiOI was calculated as 2.305×10^{-1} (the maximum degradation rate), 0.0023, and 0.1921 h^{-1}; that value substantially surpassed the values of other composites. The rate constants for the diverse photocatalysts (Table 4) can be arranged as BiOF/BiOI > BiOI ≫ BiOF. The photocatalytic activity of BiOF/BiOI composites reached a maximum rate constant of 0.2305 h^{-1}, which was 1.2 times higher than that of BiOI and 100 times higher than that of BiOF. Thus, the derived BiOF/BiOI is crucial for photocatalytic activity enhancement.

3.2.3. Durability

To investigate the durability of the BiOF/BiOI composite, this study reused some previously used samples. After each cycle, the catalyst materials were centrifuged for recovery. After the third cycle, all CV had been removed, but no apparent deficit in photocatalytic activity was observed. The observed deficit was 8.2% in the fifth run (Fig. 7(a)). XRD data revealed no differences between the previously used sample and the as-prepared sample (Fig. 7(b)), indicating the very high photostability of the BiOF/BiOI composite.

The superior photocatalytic activities of BiOF/BiOI may be attributable to synergistic effects that may include a layered structure, a low-energy band structure, a high BET surface area, and the formation of composites (or heterojunctions). When no photocatalysts were used, and CV was irradiated with visible light, the CV

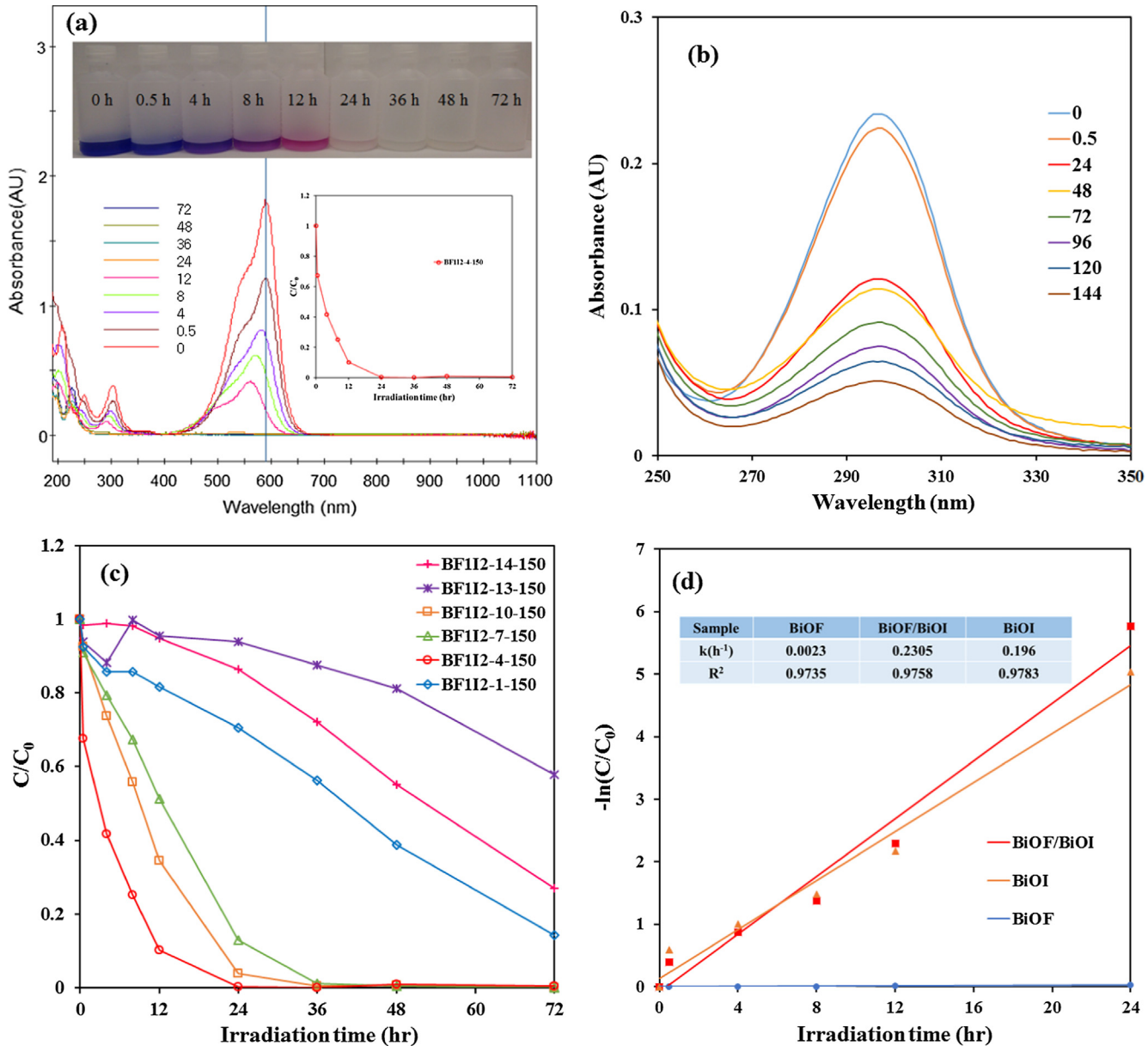

Fig. 6. Temporal UV–vis adsorption spectral of (a) CV and (b) SA, and (c, d) photocatalytic degradation of CV as a function of irradiation time over different photocatalysts (hydrothermal condition: molar ratio KF/KI = 1/2, pH = 1–14, reaction temperature = 150 °C, reaction time 12 h; 10 mg/100 mL photocatalyst, 10 ppm CV).

did not degrade. The BiOF/BiOI composites' photocatalytic superiority relative to the other composites is ascribable to the efficient utilization of visible light and efficient electron–hole separation.

3.3. Photocatalytic mechanisms

Typically, the photodegradation of organisms through a semiconductor involves photocatalysis, photolysis, and dye photosensitization [27]. Photocatalytic decomposition events in UV–Vis and semiconductor systems tend to produce various primary active species, including hydroxyl, superoxide, and hydrogen radicals ($H^{\cdot}$), as well as singlet oxygen and holes. Water dissociates on the surface of TiO_2 and in the molecular layers below the surface. Thus, Dimitrijevic et al. [28] posited that water can serve as a charge stabilizer, by preventing electron–hole recombination; that water can form H atoms and function as an electron acceptor by reacting photogenerated electrons with surface protons, $—OH_2^+$; and that water can function as an electron donor, reacting with photogenerated holes to yield ·OH radicals.

Whereas photocatalysts produce electron–hole pairs directly after illumination in the photocatalytic process, their photocatalytic efficiency mainly hinges on the recombination rate or the lifetime of the photogenerated electron–hole pairs. PL spectra were thus employed in this study to explore the photogenerated electron–hole pairs' recombination rate; they were also measured to explore the photogenerated carriers' separation capacity in the BiO_pF_q/BiO_xI_y, BiOF, and BiOI heterostructures (Fig. 8). The as-prepared materials exhibited a weak emission peak of approximately 360–500 nm, possibly engendered by the direct electron–hole recombination of band transitions. The characteristic emission peak at the lowest intensity range of 440–520 nm for the BiO_pF_q/BiO_xI_y evinces strikingly inhibited recombination of the photogenerated charge carriers. Conversely, efficient segregation might prolong the charge carrier lifespan and fortify the effectiveness of interfacial charge transfers to the adsorbed substrates, to

the great benefit of the photocatalytic activity [12]. The PL intensities observed for the BiO_pF_q/BiO_xI_y composites were relatively low, as depicted in Fig. 8(a), suggesting that their electron–hole recombination rate was meager, which also results in higher photocatalytic activity (see Fig. 6, Fig. S4, and Table 4). Moreover, the PL of Fig. 8(b) results confirm that the composites are crucial to hindering electron–hole recombination, explaining why the BiOF/BiOI composites could offer increasing photocatalytic performance. Therefore, BiOF/BiOI photocatalysts show great and slight increase, compared with BiOF and BiOI in the separation extent and lifetime of the photogenerated electrons, leading to the effective photodegradation of CV under visible light irradiation.

Bai et al. [29] argued that the trapping of active species (including superoxide ($O_2^{-}\cdot$) and hydroxyl (·OH) radicals) must be measured for catalyzing methylene blue degradation with $ZnWO_4$/graphene hybrids. Wang et al. [30] reported that $O_2^{-}\cdot$ and ·OH are the primary reactive species for degrading rhodamine B with $BiVO_4$/rGO. HO· could only be formed through the $e^- \rightarrow O_2^{-}\cdot \rightarrow H_2O_2 \rightarrow$ ·OH route. A study reported that ·OH radicals formed through the multistep $O_2^{-}\cdot$ reduction [22]. Another study [29] claimed that, instead of ·OH, e^-, or h^+, $O_2^{-}\cdot$ mainly regulated the photocatalytic process. Lee et al. [5] claimed that oxidation dominated the visible-light degradation of CV with BiO_mX_n/BiO_pY_q (X, Y = Cl, Br, and I); they identified the major active species as $O_2^{-}\cdot$ and the minor active species as ·OH and h^+. The previously discussed studies [22,29,30] have reported that with the probability of ·OH formation is notably lower than that of $O_2^{-}\cdot$ formation, but ·OH is very robust and nonselective; ·OH partially or completely mineralizes numerous organic chemicals.

By introducing several quenchers, this study reexamined the action of active species in the photocatalytic reaction process; thus, the relevant active species were scavenged. The introduction of AO, IPA, and SA did not influence the photocatalytic degradation of CV (Fig. 9(a)); however, the quenching of BQ, obviously diminished the efficiency of the degradation. In CV photocatalytic degradation, O_2^{-} is a major active species. As indicated in Fig. 9(b) and (c), when the reaction was executed in darkness, no and triplet ($^1O_2$) EPR signals were noted, respectively. However, when the reaction process was conducted under irradiation provided by visible light, intensity signals corresponding to the characteristic peak of DMPO-·OH adducts (Fig. 9(b)) were not noted, and prolonging the reaction time resulted in an unobviously increase in the intensity; conversely, when the reaction process was conducted under irradiation provided by visible light, DMPO-$O_2^{-}\cdot$ adducts (Fig. 9(c)) were noted, and prolonging the reaction time resulted in a gradual increase in the intensity. This suggests that the O_2^{-} (main active species) was formed in the presence of BiOF/BiOI and oxygen under irradiation provided by visible light. Thus, the quenching effects induced by scavengers and by EPR prove that O_2^{-} is crucial in this degradation, whereas $^1O_2$ species are involved, but not crucial.

The structure characterizations have proven that BiOF/BiOI is a two-phase heterojunction. Considering that the heterojunction presents much higher photocatalytic activities than the component phase alone, it is reasonable that there might be synergetic effect between BiOF and BiOI. Actually, many researchers have noted

Table 4
Pseudo-first-order rate constants for the degradation of CV with photocatalysts under visible light irradiation. (Hydrothermal conditions: molar ratio KF/KI = 1/2–2/1, temp = 100–250 °C, pH = 1–14, time = 12 h).

Sample	k (h^{-1})	R^2	Sample	k (h^{-1})	R^2
BF1I2-1-100	0.0561	0.9851	BF2I1-1-100	0.002	0.8524
BF1I2-4-100	0.1952	0.9871	BF2I1-4-100	0.2169	0.955
BF1I2-7-100	0.0563	0.9809	BF2I1-7-100	0.0955	0.9635
BF1I2-10-100	0.0696	0.9940	BF2I1-10-100	0.0622	0.9758
BF1I2-13-100	0.0339	0.9378	BF2I1-13-100	0.0037	0.809
BF1I2-14-100	0.0043	0.8343	BF2I1-14-100	0.0028	0.4748
BF1I2-1-150	0.0125	0.98189	BF2I1-1-150	0.0009	0.0326
BF1I2-4-150	**0.2305**	**0.9758**	BF2I1-4-150	0.1431	0.9833
BF1I2-7-150	0.0824	0.9523	BF2I1-7-150	0.0336	0.9598
BF1I2-10-150	0.1323	0.9549	BF2I1-10-150	0.0967	0.9917
BF1I2-13-150	0.0005	0.0091	BF2I1-13-150	0.0023	0.1389
BF1I2-14-150	0.0058	0.9245	BF2I1-14-150	0.0005	0.0162
BF1I2-1-200	0.017	0.9969	BF2I1-1-200	0.0013	0.0018
BF1I2-4-200	0.2206	0.9436	BF2I1-4-200	0.1012	0.9406
BF1I2-7-200	0.0898	0.9618	BF2I1-7-200	0.2298	0.9391
BF1I2-10-200	0.1754	0.9406	BF2I1-10-200	0.1199	0.9523
BF1I2-13-200	0.0045	0.5689	BF2I1-13-200	0.0014	0.5276
BF1I2-14-200	0.0043	0.8284	BF2I1-14-200	0.0174	0.9116
BF1I2-1-250	0.0572	0.9831	BF2I1-1-250	0.0065	0.9649
BF1I2-4-250	0.1765	0.9835	BF2I1-4-250	0.2104	0.9532
BF1I2-7-250	0.14	0.9721	BF2I1-7-250	0.053	0.9416
BF1I2-10-250	0.1252	0.9821	BF2I1-10-250	0.005	0.8324
BF1I2-13-250	0.003	0.5143	BF2I1-13-250	0.0401	0.8371
BF1I2-14-250	0.0085	0.9064	BF2I1-14-250	0.0065	0.9612
BiOF	0.0023	0.9125	BiOI	0.1921	0.9837

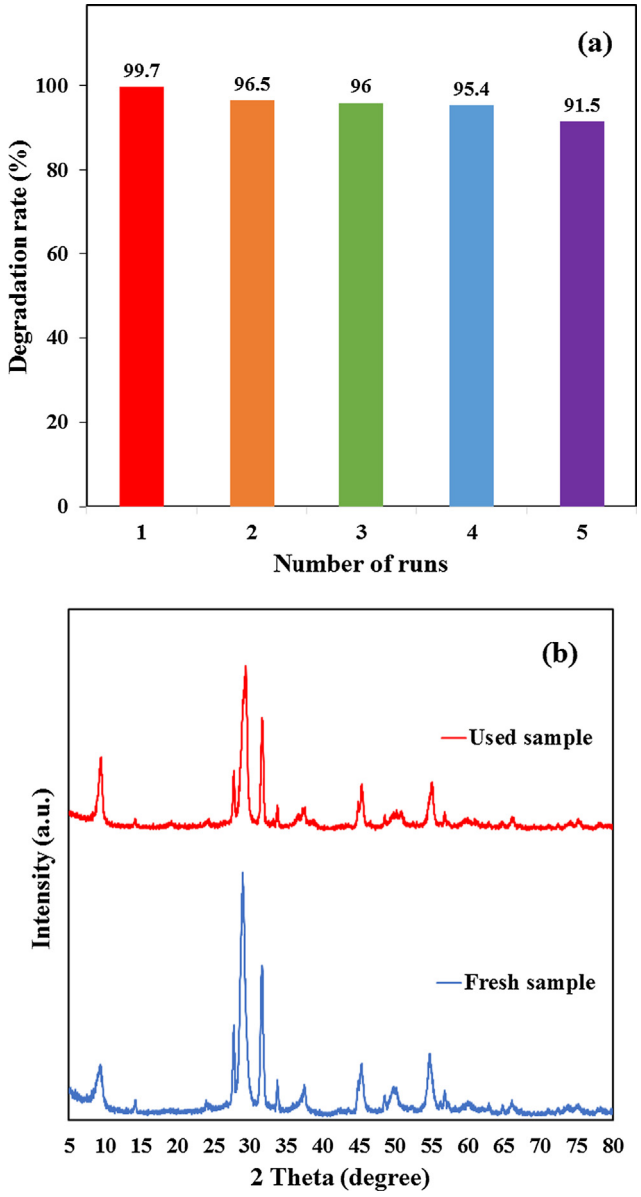

Fig. 7. (a) Cycling runs and (b) XRD patterns acquired before and after in the photocatalytic degradation of CV in the presence of BiOF/BiOI.

the synergetic effect in heterojunction systems consisting of two semiconductors in contact [31,32] and attributed the effect to the efficient charge transfer at the interface of two semiconductors, which would result in an effective photoexcited electron–hole separation and, consequently, enhance the photocatalytic activity. The driving force of charge transfer originates from the matching band potentials. Therefore, the suitable band potential is the precondition for the synergetic effect of heterojunction photocatalysts. Typically for $V_2O_5/BiVO_4$ heterostructured photocatalysts [33], the conduction-band (CB) potential level of $BiVO_4$ is more negative than that of V_2O_5 so that photogenerated electrons could migrate from $BiVO_4$ to V_2O_5 driven by the contact electric field. Fig. 10 shows the type-I heterostructure band alignment [32]. In the type-I band alignment, both VB and CB edges of BiOI are localized within the energy gap of BiOF, forming the straddling band alignment. The VB and CB potentials of two different semiconductors play a crucial role in the determination of the physical features

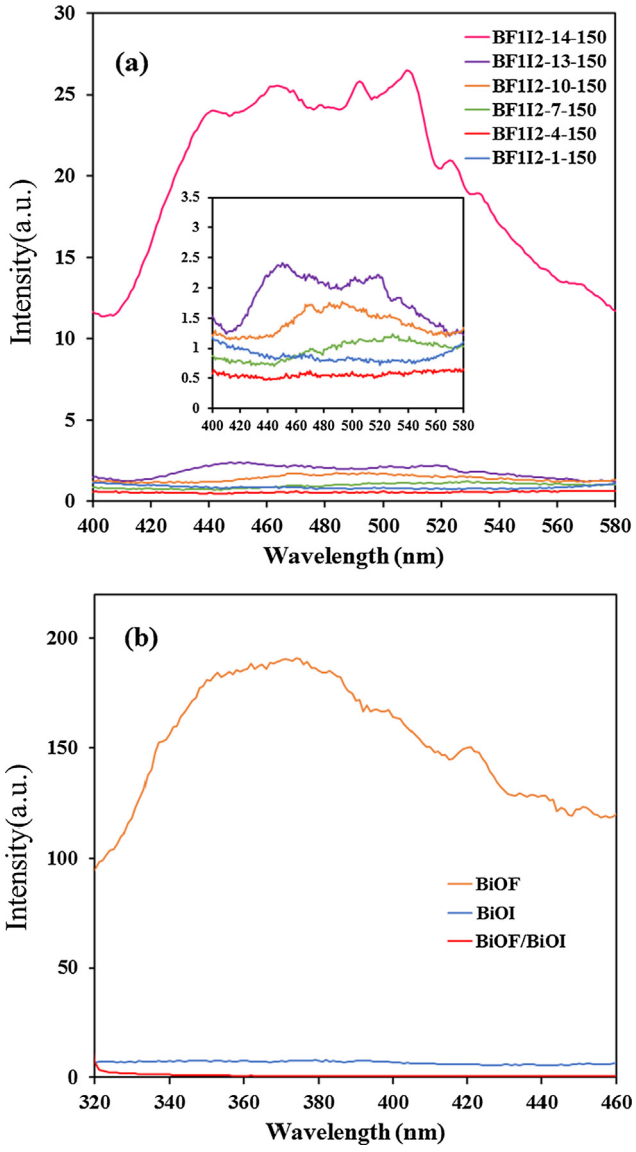

Fig. 8. PL spectra of (a) as-prepared BiO_pF_q/BiO_xI_y samples at different pH values and (b) BiOF, BiOI, and BiOF/BiOI (hydrothermal conditions: molar ratio KF/KI = 1/2; temp = 150 °C; time = 12 h).

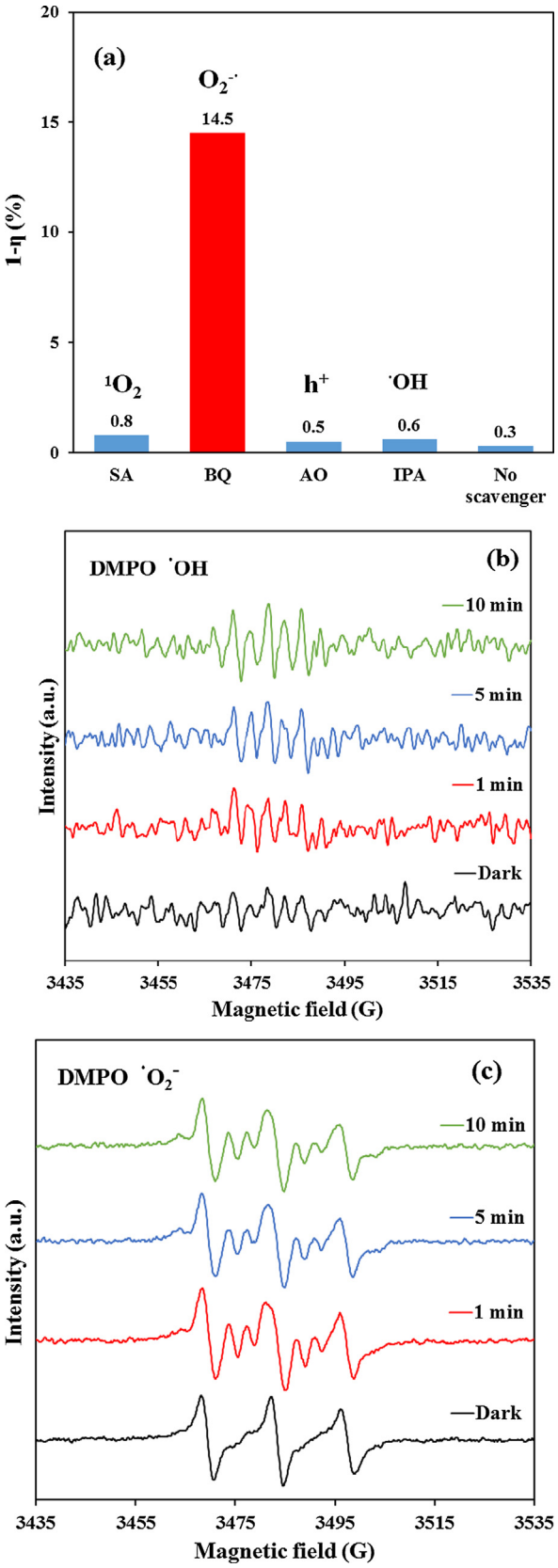

Fig. 9. (a) CV concentration during photodegradation as a function of irradiation time observed in BiOF/BiOI under the addition of different scavengers: SA, IPA, AQ, and BQ. EPR spectra for (a) DMPO-$^{\cdot}OH$ and (b) DMPO-$^{\cdot}O_2^-$ under visible-light irradiation with BiOF/BiOI.

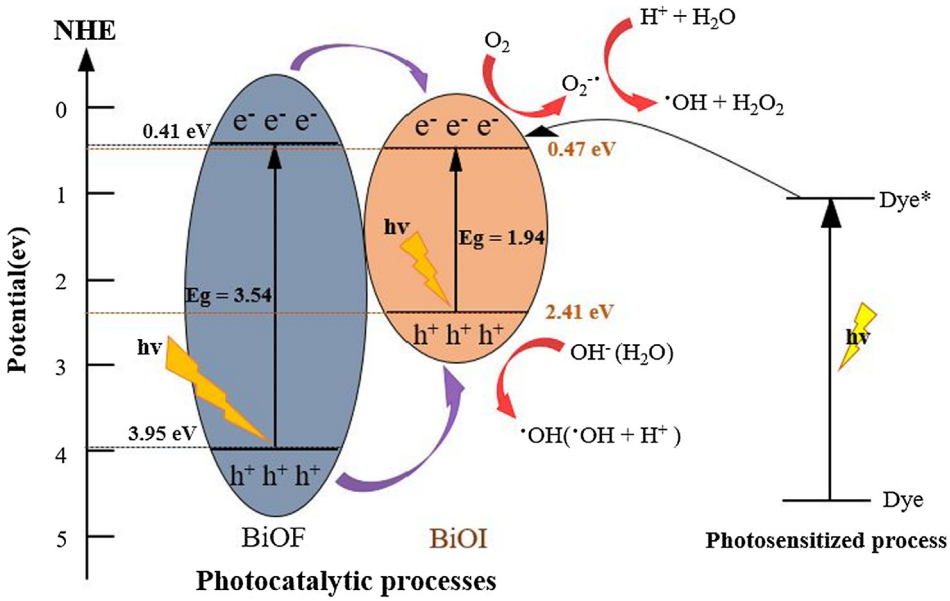

Fig. 10. Schematic of the bandgap structures of BiOF/BiOI and the possible charge separation processes.

of photogenerated charges and the photocatalytic performance. BiOF/BiOI heterostructured photocatalysts, the CB potential level of BiOF, is more negative than that of BiOI so that photogenerated electrons could migrate from BiOF to BiOI driven by the contact electric field. As the CB potentials of BiOF (0.41 eV) and BiOI (0.47 eV) are a little different, the photoexcited electron is easy to transfer from the CB of BiOF to the CB of BiOI; and, the VB potentials of BiOF (3.95 eV) and BiOI (2.41 eV) are also a little different that the photoexcited holes are easy to transfer from the VB of BiOF to the VB of BiOI. Although both photogenerated charge carries were transferred from BiOF to BiOI through the interface, the difference between the migration rates of electrons and holes leads to efficient separation of the charge carriers at the interface. Moreover, the unique configuration of BiOF/BiOI allowed both charge carriers to exposing to the liquid phase and effectively involving in the photocatalytic reactions to resulting in the improvement of photocatalytic activity. For the BiOI, photoexcited carriers very easily transfer to the surface-trap states typically located within the semiconductor bandgap, on which the electrons or the holes with lower energy, and were unuseful for the redox reactions [37,38]. Therefore, BiOF/BiOI photocatalysts show great increase in the separation extent and lifetime of the photogenerated electrons, leading to the effective photodegradation of CV under visible-light irradiation.

Based on the above investigation, a possible mechanism for the photocatalysis and photosensitized processes by the BiOF/BiOI composites can be illustrated in Fig. 10. On reaching the BiOX (X = F, I) conduction band, an electron causes active oxygen species formation, which causes CV dye decomposition. Photosensitized and photocatalytic processes both operate at the same time (Fig. 10). In photosensitized and photocatalytic reactions, photogenerated and photosensitized electrons react with photocatalyst-surface-dwelling oxygen to produce $O_2^{\cdot-}$ radicals. Also, $O_2^{\cdot-}$ radicals react with H^+ ions and h^+ holes react with OH^- ions (or H_2O) to generate hydroxyl radicals. These processes produce hydroxyl radicals [34]. Interestingly, the ongoing addition of visible light sustains this cycle continuously [3]. To understand this, consider the mechanism of $^1O_2$ formation during the photoexcitation of BiOF/BiOI photocatalyst. Given suitable oxidizing power, $^1O_2$ can also be produced by transferring electrons between superoxide $O_2^{\cdot-}$ and cation species [35]. Photogenerated h^+ can function as a cation species that oxidizes $O_2^{\cdot-}$ in semiconductor nanoparticles. A published article [36] has reported this $^1O_2$ production mechanism during ZnO photoexcitation; Eqs. (15) and (16) present the CV decomposition caused by the derived oxidant species after several photo-oxidation cycles.

$$CV + O_2^{\cdot-} \rightarrow \text{decomposed compounds} \quad (15)$$

$$CV + {}^1O_2 \rightarrow \text{decomposed compounds} \quad (16)$$

This study specified hydroxylated compounds for visible-light photocatalytic degradation of CV in semiconductor systems [5]. Under UV irradiation, nitrogen-centered radical production preceded *N*-dealkylation, and carbon-centered radical establishment preceded dye chromophore structure demolition in the photocatalytic degradation of CV dye [2,3,34]. All the identified intermediates in these two topics were identical under UV light and visible light. The photocatalytic and photosensitized processes operate concurrently; nevertheless, $O_2^{\cdot-}$ is produced from the reaction on the photocatalyst surface, of O_2 with photogenerated and photosensitized e^-, and ·OH is produced from $O_2^{\cdot-}$–H^+ and h^+–OH^- (or H_2O) reactions. Notably, the hydroxyl radical (HO·) is probably generated only through the $e^- \rightarrow O_2^{\cdot-} \rightarrow H_2O_2 \rightarrow$ ·OH route, whereas the ·OH radical is produced through a multistep $O_2^{\cdot-}$ reduction. The major oxidants are ·OH radicals rather than $O_2^{\cdot-}$ radicals. Information regarding the reaction pathways of the proposed BiOF/BiOI-mediated photocatalytic processes can be used to optimize dye decomposition operations.

4. Conclusions

This is the first study to apply a facile hydrothermal process for BiO_pF_q/BiO_xI_y-mediated CV dye photocatalytic degradation under visible-light irradiation. Excellent photocatalytic activity was observed for the synthesized BiOF/BiOI composite during degradation. In terms of rate constants, the composites were sorted in the following order: BiOF/BiOI > BiOI ≫ BiOF. The maximum rate constant of the BiOF/BiOI photocatalytic activity was 0.2305 h^{-1}, 1.2 times higher than that of BiOF and 100 times higher than that of BiOF. Thus, the derived BiOF/BiOI is paramount for improving the photocatalytic activity. After the removal of CV in the third cycle,

the study did not observe any apparent deficit in photocatalytic activity, and the observed deficit was 8.2% during the fifth run. Many scavengers caused quenching effects, proving the highly influential role of the reactive $O_2^{\bullet-}$ species in the degradation of the CV used. In sum, adequate catalytic activity and stability were observed for the proposed composites; the proposed composites are highly effective heterogeneous photocatalysts energized by visible light for efficient organic pollutant degradation.

Acknowledgments

This research was supported by the Ministry of Science and Technology of the Republic of China (MOST-106-2113-M-142-001).

References

[1] M. Kubacka, Fernández-García, G. Colón, Advanced nanoarchitectures for solar photocatalytic applications, Chem. Rev. 112 (2012) 1555–1614.
[2] Y.R. Jiang, H.P. Lin, W.H. Chung, Y.M. Dai, W.Y. Lin, C.C. Chen, Controlled hydrothermal synthesis of BiO_xCl_y/BiO_mI_n composites exhibiting visible-light photocatalytic degradation of crystal violet, J. Hazard. Mat. 283 (2015) 787–805.
[3] Y.R. Jiang, S.Y. Chou, J.L. Chang, S.T. Huang, H.P. Lin, C.C. Chen, Hydrothermal synthesis of bismuth oxybromide-bismuth oxyiodide composites with highly visible light photocatalytic performance for the degradation of CV and phenol, RSC Adv. 5 (2015) 30851–30860.
[4] W.L.W. Lee, W.H. Chung, W.S. Huang, W.C. Lin, W.Y. Lin, Y.R. Jiang, C.C. Chen, Photocatalytic activity and mechanism of nano-cubic barium titanate prepared by a hydrothermal method, J. Taiwan Inst. Chem. Eng. 44 (2013) 660–669.
[5] W.W. Lee, C.S. Lu, C.W. Chuang, Y.J. Chen, J.Y. Fu, C.W. Siao, C.C. Chen, Synthesis of bismuth oxyiodides and their composites: characterization, photocatalytic activity, and degradation mechanisms, RSC Adv. 5 (2015) 23450–23463.
[6] W.L.W. Lee, J.S. Lin, J.L. Chang, J.Y. Chen, M.C. Cheng, C.C. Chen, Photodegradation of CV over nanocrystalline bismuth tungstate prepared by hydrothermal synthesis, J. Mol. Catal. A: Chem. 361–362 (2012) 80–90.
[7] K. Yu, S. Yang, C. Liu, H. Chen, H. Li, C. Sun, S.A. Boyd, Degradation of organic dyes via bismuth silver oxide initiated direct oxidation coupled with sodium bismuthate based visible light photocatalysis, Environ. Sci. Technol. 46 (2012) 7318–7326.
[8] S.Y. Chou, W.H. Chung, L.W. Chen, Y.M. Dai, W.Y. Lin, J.H. Lin, C.C. Chen, A series of BiO_xI_y/GO photocatalysts: synthesis, characterization, activity, and mechanism, RSC Adv. 6 (2016) 82743–82758.
[9] C.T. Yang, W.W. Lee, H.P. Lin, Y.M. Dai, H.T. Chi, C.C. Chen, A novel heterojunction Bi_2SiO_5/g-C_3N_4: synthesis, characterization, photocatalytic activity, and mechanism, RSC Adv. 6 (2016) 40664–40675.
[10] H.P. Lin, C.C. Chen, W.W. Lee, Y.Y. Lai, J.Y. Chen, Y.Q. Chen, J.Y. Fu, Synthesis of $SrFeO_{3-x}$/g-C_3N_4 heterojunction with improved visible-light photocatalytic activities in chloramphenicol and crystal violet degradation, RSC Adv. 6 (2016) 2323–2336.
[11] J. Li, Y. Yu, L. Zhang, Bismuth oxyhalide nanomaterials: layered structures meet photocatalysis, Nanoscale 6 (2014) 8473–8488.
[12] X. Xiao, C. Xing, G. He, X. Zuo, J. Nan, L. Wang, Solvothermal synthesis of novel hierarchical $Bi_4O_5I_2$ nanoflakes with highly visible light photocatalytic performance for the degradation of 4-tert-butylphenol, Appl. Catal. B: Environ. 148–149 (2014) 154–163.
[13] W. Su, J. Wang, Y. Huang, W. Wang, P. Liu, Synthesis and catalytic performances of a novel photocatalyst BiOF, Scripta Mater. 62 (2010) 345–348.
[14] M. Ren, F. Teng, Y. Yang, Y. Zhai, Y. Teng, Influence of O/F ratio on oxygen defect and photochemical properties of $Bi_xO_yF_z$, Mater. Des. 131 (2017) 402–409.
[15] J. Cheng, L. Frezet, P. Bonnet, C. Wang, Preparation and photocatalytic properties of a hierarchical BiOCl/BiOF composite photocatalyst, Catal. Lett. 148 (2018) 1281–1288.
[16] T. Jiang, J. Li, Y. Gao, L. Li, L. Pan, BiOBr/BiOF composites for efficient degradation of rhodamine B and nitrobenzene under visible light irradiation, J. Colloid Interface Sci. 490 (2017) 812–818.
[17] W.L. Huang, Q.S. Zhu, DFT calculations on the electronic structures of BiOX (X = F, Cl, Br, I) photocatalysts with and without semicore Bi 5d states, J. Comput. Chem. 30 (2009) 183–190.
[18] X. Xiao, C. Liu, R. Hu, X. Zuo, J. Nan, L. Li, L. Wang, Oxygen-rich bismuth oxyhalides: generalized one-pot synthesis, band structures and visible-light photocatalytic properties, J. Mater. Chem. 22 (2012) 22840–22843.
[19] E. Keller, V. Kramer, A strong deviation from Vegard's rule: x-ray powder investigations of the three quasi-binary phase systems BiOX-BiOY (X,Y = Cl, Br, I), Z. Naturforsch. 60b (2005) 1255–1263.
[20] X. Xiao, W.D. Zhang, Hierarchical $Bi_7O_9I_3$ micro/nano-architecture: facile synthesis, growth mechanism, and high visible light photocatalytic performance, RSC Adv. 1 (2011) 1099–1105.
[21] W.W. Lee, C.S. Lu, C.W. Chuang, Y.J. Chen, J.Y. Fu, C.W. Siao, C.C. Chen, Synthesis of bismuth oxyiodides and theircomposites: characterization, photocatalytic activity, and degradation mechanisms, RSC Adv. 5 (2015) 23450–23463.
[22] S.T. Huang, Y.R. Jiang, S.Y. Chou, Y.M. Dai, C.C. Chen, Synthesis, characterization, photocatalytic activity of visible-light-responsive photocatalysts BiO_xCl_y/BiO_mBr_n by controlled hydrothermal method, J. Mol. Catal. A: Chem. 391 (2014) 105–120.
[23] K.L. Li, W.W. Lee, C.S. Lu, Y.M. Dai, S.Y. Chou, M.C. Wang, C.C. Chen, Synthesis of BiOBr, Bi_3O_4Br, and $Bi_{12}O_{17}Br$ 2 by controlled hydrothermal method and their photocatalytic properties, J. Taiwan Inst. Chem. Eng. 45 (2014) 2688–2697.
[24] H.L. Chen, W.W. Lee, W.H. Chung, Y.J. Chen, Y.R. Jiang, H.P. Lin, W.Y. Lin, C.C. Chen, Controlled hydrothermal synthesis of bismuth oxybromides and their photocatalytic properties, J. Taiwan Inst. Chem. Eng. 45 (2014) 1892–1909.
[25] F. Dong, Y. Sun, M. Fu, Z. Wu, S.C. Lee, Room temperature synthesis and highly enhanced visible light photocatalytic activity of porous BiOI/BiOCl composites nanoplates microflowers, J. Hazard. Mater. 219–220 (2012) 26–34.
[26] A. Chatzitakis, C. Berberidou, I. Paspaltsis, G. Kyriakou, T. Sklaviadis, I. Poulios, Photocatalytic degradation and drug activity reduction of chloramphenicol, Water Res. 42 (2008) 386–394.
[27] C. Nasr, K. Vinodgopal, L. Fisher, S. Hotchandani, A.K. Chattopadhyay, P.V. Kamat, Environmental photochemistry on semiconductor surfaces. Visible light induced degradation of a textile diazo dye, naphthol blue black, on TiO_2 nanoparticles, J. Phys. Chem. 100 (1996) 8436–8442.
[28] N.M. Dimitrijevic, B.K. Vijayan, O.G. Poluektov, T. Rajh, K.A. Gray, H. He, P. Zapol, Role of water and carbonates in photocatalytic transformation of CO_2 to CH_4 on Titania, J. Am. Chem. Soc. 133 (2011) 3964–3971.
[29] X. Bai, L. Wang, Y. Zhu, Visible photocatalytic activity enhancement of $ZnWO_4$ by graphene hybridization, ACS Catal. 2 (2012) 2769–2778.
[30] Y. Wang, W. Wang, H. Mao, Y. Lu, J. Lu, J. Huang, Z. Ye, B. Lu, Electrostatic self-assembly of $BiVO_4$–reduced graphene oxide nanocomposites for highly efficient visible light photocatalytic activities, ACS Appl. Mater. Interfaces 6 (2014) 12698–12706.
[31] H. Li, Y. Zhou, W. Tu, J. Ye, Z. Zou, State-of-the-art progress in diverse heterostructured photocatalysts toward promoting photocatalytic performance, Adv. Funct. Mater. 25 (2015) 998–1013.
[32] Z. Li, J. Feng, S. Yan, Z. Zou, Solar fuel production: strategies and new opportunities with nanostructures, Nano Today 10 (2015) 468–486.
[33] J. Su, X.X. Zou, G.D. Li, X. Wei, C. Yan, Y.N. Wang, J. Zhao, L.J. Zhou, J.S. Chen, Macroporous V_2O_5–$BiVO_4$ composites: effect of heterojunction on the behavior of photogenerated charges, J. Phys. Chem. C 115 (2011) 8064–8071.
[34] H.J. Fan, C.S. Lu, W.L.W. Lee, M.R. Chiou, C.C. Chen, Mechanistic pathways differences between P25-TiO_2 and Pt-TiO_2 mediated CV photodegradation, J. Hazard. Mater. 185 (2011) 227–235.
[35] W. He, H. Jia, W.G. Wamer, Z. Zheng, P. Li, J.H. Callahan, J.J. Yin, Predicting and identifying reactive oxygen species and electrons for photocatalytic metal sulfide micro–nano structures, J. Catal. 320 (2014) 97–105.
[36] W. He, H.K. Kim, W.G. Wamer, D. Melka, J.H. Callahan, J.J. Yin, Photogenerated charge carriers and reactive oxygen species in ZnO/Au hybrid nanostructures with enhanced photocatalytic and antibacterial activity, J. Am. Chem. Soc. 136 (2014) 750–757.
[37] L. Huang, X.L. Wang, J.H. Yang, G. Liu, J.F. Han, C. Li, Dual cocatalysts loaded type I CdS/ZnS core/shell nanocrystals as effective and stable photocatalysts for H_2 evolution, J. Phys. Chem. C 117 (2013) 11584–11591.
[38] L. Huang, J.H. Yang, X.L. Wang, J. Han, H.X. Han, C. Li, Effects of surface modification on photocatalytic activity of CdS nanocrystals studied by photoluminescence spectroscopy, Phys. Chem. Chem. Phys. 15 (2013) 553–560.